PHYSICAL REVIEW B VOLUME 47, NUMBER 16 15 APRIL 1993-II

Elasto-optical constants of Si

P. Etchegoin, J. Kircher,* and M. Cardona
Max-Planck-Institut für Festkörperforschung, Heisenbergstrasse 1, D-7000 Stuttgart 80, Germany
(Received 4 November 1992)

The three independent components of the piezo-optical tensor $P_{ijkl}(\omega)$ have been determined in uniaxially stressed Si using rotating-analyzer ellipsometry. This tensor, with only three complex independent components in the case of Si, links the changes in the real and imaginary parts of the dielectric tensor $\Delta\epsilon_{ij}(\omega)$ to an arbitrary stress $\mathbf{X}=X_{kl}$ [i.e., $\Delta\epsilon_{ij}(\omega) = P_{ijkl}(\omega)X_{kl}$]. Using the experimental values of $P_{ijkl}(\omega)$, several related functions and parameters were derived and compared with previous piezoreflectance, ac-stress-modulated reflectivity, Raman spectroscopy work, and theoretical estimates. Deformation-potential constants for the optical transitions between 3 and 4 eV were obtained using the ellipsometric data. In addition, the different components of the piezo-optical tensor were calculated using the empirical pseudopotential method and reasonable agreement between theory and experiment was found. Our data also clarify previous problems and errors in the existing literature.

I. INTRODUCTION AND OVERVIEW

Stress in semiconductors and its relation with the optical properties[1–4] is a subject of long-standing basic interest which has been revived by the appearance of novel semiconductor structures such as strained superlattices. While the main effects observed in these systems are related to the atomic superperiodicity, others are simply produced by the presence of internal strain, caused by lattice mismatch. The latter can contribute significantly to the physical properties of the superstructure. An important ingredient for the analysis of stressed superlattices, especially their optical properties, is the detailed knowledge of the dielectric functions of the composing bulk materials under stress. However, the complex dielectric tensor $\epsilon_{ij}(\omega)$ or, equivalently, the complex index of refraction $n_{ij}(\omega)$, as a function of stress are in many cases not known. Only in some cases is qualitative information derived by way of Kramers-Kronig analysis of piezoreflectance data (with the consequent uncertainty arising from the extrapolations at low and high energies) available. This lack of information is particularly acute in the visible-uv photon energy range ($\sim 1.5 - 6$ eV) even for the most common semiconductors such as silicon. The goal of the present paper is to report an experimental determination of the so-called piezo-optical tensor $P_{ijkl}(\omega)$,[5,6] as well as to compare the data with previous related information (such as deformation potentials) and clarify some problems existing in the literature. A comparison with theoretical calculations based on the rigid ion empirical pseudopotential method (EPM), and other recent theoretical work, is presented.

This work complements previous papers on the optical properties of bulk semiconductors under stress including germanium[5] and GaAs (Ref. 6) and, for that reason, background material will be kept to a minimum. Rather than dwell on basic facts of the data evaluation and the experimental details, the reader will be referred to Refs. 5 and 6 and the discussion will be focused on the features specific to Si so as to keep the length to a minimum.

The structure of the paper is as follows. The experimental section discusses the data evaluation, results, and comparisons with previous data. The section devoted to theory shows the EPM calculations and, finally, the conclusions are presented at the end.

II. EXPERIMENT

A. Experimental technique and sample preparation

In order to measure the differential changes of the real and imaginary parts of the dielectric tensor $\Delta\epsilon_{ij}(\omega)$ as a function of applied uniaxial stress $\mathbf{X}$, we used a rotating-analyzer ellipsometer (RAE).[7–9] The instrument can be employed as a tool to obtain the projection of the dielectric tensor along the line defined by the intersection of the plane of incidence and the sample surface.[10] The experimental method to obtain the piezo-optical components of the tensor, starting from the ellipsometric measurements, is identical to that explained in Refs. 5 and 6, where a detailed description of the setup and the analysis of errors can be found.[11] The stress apparatus used for the optical measurements is detailed elsewhere.[12] We use the same conventions of symbols and signs as in Refs. 5 and 6.

The samples used in the present work were high-purity n-type Si ($\rho \sim 800$ Ωcm at room temperature), with typical dimensions $1.8\times2.8\times18$ mm^3, oriented with the longest side along [111] or [100], respectively. The surfaces were mechanically polished and chemically etched before the experiment using 0.02 vol. % bromine in methanol, 1:1 NH_4OH:H_2O and 5 vol. % HF in methanol as suggested in Refs. 13 and 14.

 ©1993 The American Physical Society

B. Experimental results and discussion

The starting point of our experiments is the ellipsometric determination of the pseudodielectric function of unstressed bulk Si at room temperature (RT), which is shown in Fig. 1 (lines). The data have been corrected for a SiO_2 oxide layer of $\sim$10 Å. The symbols in Fig. 1 represent data from Ref. 13 taken within a windowless etchcell in a N_2 atmosphere on a very clean surface. These data from Ref. 13 are used as reference values to take into account the effect of an oxide layer on the surface of our samples. Data of the pseudodielectric function of epitaxial Si surfaces have been recently reported in Ref. 15. The comparison between our results and those of Ref. 13 for Si is similar to that shown for GaAs and Ge in Refs. 5 and 6. Applying a compressive uniaxial stress along [111] or [100] up to $\sim$ 20 kbars= 2 GPa, and measuring the parallel ($\|$) and perpendicular ($\perp$) components of $\epsilon_{ij}(\omega)$ with respect to the stress ($\mathbf{X}$), it is possible to obtain the three independent components of $P_{ijkl}(\omega)$, i.e., $P_{11}(\omega)$, $P_{12}(\omega)$, and $P_{44}(\omega)$. The different configurations and the possible results according to every particular geometry were given in Refs. 5 and 6, and can also be found in Ref. 4. In Fig. 2 we show the three independent components of $P_{ijkl}(\omega)$ with their real and imaginary parts. The Kramers-Kronig consistency[5,6] between the real and imaginary parts of each component of $P_{ijkl}(\omega)$ was checked using the experimental imaginary part and calculating the corresponding real part with the use of Eq. (14) of Ref. 5 (dashed curves accompanying the real parts in Fig. 2). The consistency is satisfactory for all components of $P_{ijkl}(\omega)$. Typical error bars are shown in Fig. 2 for some photon energies; they were obtained as in Refs. 5 and 6. These are the basic experimental result of the present paper. In Fig. 3 we show two of the linear combinations that are irreducible components of the piezo-optical tensor, i.e., $[P_{11}(\omega) + 2P_{12}(\omega)]$, which represents the hydrostatic part transforming like Γ_1 and $[P_{11}(\omega) - P_{12}(\omega)]$ that transforms like Γ_{12}. The third irreducible component $P_{44}(\omega)$, already shown in Fig. 2(c), transforms like $\Gamma_{25'}$. The data of Fig. 3 were obtained directly from the data of Fig. 2 by computing the appropriate linear combination.

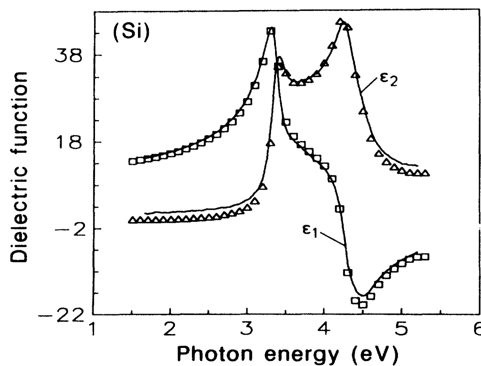

FIG. 1. Real $[\epsilon_1(\omega)]$ and imaginary $[\epsilon_2(\omega)]$ parts of the pseudodielectric function of bulk Si at room temperature without stress. The data have been corrected for an oxide layer (SiO_2) of $\sim$10 Å. The solid symbols are data from Ref. 13 on a very clean surface maintained in a N_2 atmosphere (see also Ref. 15).

The curves displayed in Fig. 2 can be used to simulate several piezo-optical response functions by means of simple numerical manipulation. They can be used later to compare with existing data from other related experiments. In Fig. 4 we show a comparison of this kind. The five curves in Fig. 4 correspond to several differential changes in the reflectivity $\Delta R(\omega)/R(\omega)$ for $\mathbf{X}$ along [110] or [001] and polarizations parallel ($\|$) or perpendicular ($\perp$) to the stress. For $\mathbf{X}\|[110]$ and polarization of the light $\|$ to $[1\bar{1}0]$, the change in the projection of the dielectric tensor along this direction is given by

$$\Delta\epsilon_{[110]}^{[1\bar{1}0]}(\omega) = [P_{11}(\omega) + P_{12}(\omega) + P_{44}(\omega)]\ X, \tag{1}$$

where the subscript of $\epsilon(\omega)$ indicates the direction of $\mathbf{X}$, X its magnitude, and the superscript the direction of the electric field of the light ($\mathbf{E}$). Using (1), the related change $\Delta R(\omega)/R(\omega)$ can be calculated by means of Eq. (3) of Ref. 5, making use of the experimental values of $P_{ijkl}(\omega)$ shown in Fig. 2. The result obtained with Eq. (1) is plotted in Fig. 4(a) (Pol. $\perp$). The curve labeled (Pol. $\|$) in Fig. 4(a) corresponds to parallel polarization along [110] and was calculated using

$$\Delta\epsilon_{[110]}^{[110]}(\omega) = [P_{11}(\omega) + P_{12}(\omega) - P_{44}(\omega)]\ X. \tag{2}$$

The inset at the top of Fig. 4 shows the same two results obtained with ac-stress modulation of the reflectivity in Ref. 16. Figure 4(b) shows the other possible perpendicular polarization ($\mathbf{E}$ along [001]) for $\mathbf{X}\|[110]$. In this case $\Delta\epsilon_{[110]}^{[001]}(\omega) \propto P_{12}(\omega)$. The inset in the middle of the figure displays data from Ref. 16 corresponding to this configuration. Figure 4(c) shows the case of $\mathbf{X}\|[001]$ for $\|$ and $\perp$ polarizations. The inset at the bottom exhibits the equivalent data from Ref. 16. In these two last cases we have $\Delta\epsilon_{[001]}^{[001]}(\omega) \propto P_{11}(\omega)$ and $\Delta\epsilon_{[100]}^{[001]}(\omega) \propto P_{12}(\omega)$, respectively. In Ref. 16 three fundamental piezoreflectance functions [equivalent to our $P_{ijkl}(\omega)$ tensor] were given. However, the evaluation of these functions seems to have been incorrect. The same problem was found with the data shown in Ref. 17. Although the procedure to calculate the piezo-optical components was in principle correct, the lack of an absolute zero in piezoreflectance experiments produces considerable errors. For example, $P_{44}(\omega)$ in Ref. 17 was calculated by Kramers-Kronig analysis of the difference between the curves shown in the inset of Fig. 4(a). However, this implies the subtraction of data from two different experiments and produces problems with the numerical analysis of the Kramers-Kronig integrals. Contrary to this, our data for $P_{ijkl}(\omega)$ reproduce rather well the raw piezoreflectance or ac-stress-modulated reflectivity data. In Fig. 5 we compare the absolute change in the reflectivity $R(\omega, \mathbf{X})$ for different polarizations ($\|$ or $\perp$ to $\mathbf{X}$) with polarized reflectivity data from Ref. 18. Although the stress is not exactly the same as in Ref. 18 the same qualitative trends agree. Our changes in $R(\omega)$ with $\mathbf{X}$ have been calculated using

the appropriate change in the dielectric tensor with the experimental $P_{ijkl}(\omega)$'s from Fig. 2 (see Refs. 5 and 6).

In Fig. 6 we show the low-energy tail of the real part of $[\epsilon^{\parallel}(\omega) - \epsilon^{\perp}(\omega)]/X = [P_{11}(\omega) - P_{12}(\omega)]$ (Refs. 5 and 6) for $\mathbf{X}\parallel[100]$. The full circles are a collection of experimental data from Refs. 19–23, involving direct measurement of the birefringence below the lowest (indirect) gap by transmission between parallel or crossed polarizers, and Raman scattering above that gap.[21] Open circles are theoretical *ab initio* pseudopotential calculations us-

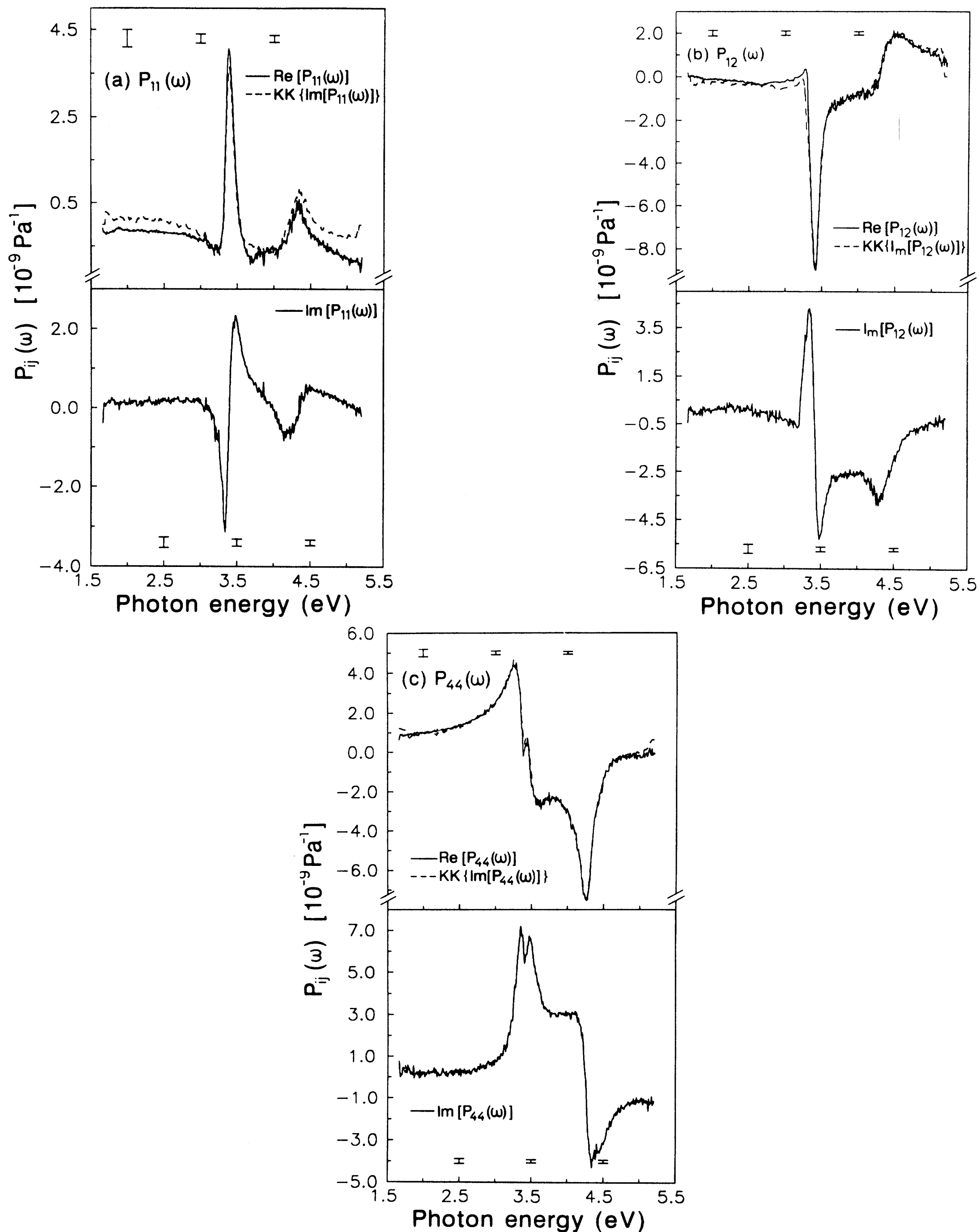

FIG. 2. Real and imaginary parts of (a) $P_{11}(\omega)$, (b) $P_{12}(\omega)$, and (c) $P_{44}(\omega)$ obtained as in Refs. 5 and 6. The real parts are shown together with the computed Kramers-Kronig curve (dashed line) utilizing the imaginary counterpart. Error bars correspond to the given photon energies and were obtained as in Refs. 5 and 6.

ing a local-density approximation (LDA) for exchange and correlation and the so-called "scissors operator."[24] Since the low-energy tail of $\mathrm{Re}[P_{11}(\omega) - P_{12}(\omega)]$ is very small, the statistical noise shown in Fig. 3(a) was too large to allow comparison with previous data. This region was measured separately 16 times, thus reducing the statistical noise by a factor of 4. The inset of Fig. 6 shows explicitly $\mathrm{Re}[P_{11}(\omega) - P_{12}(\omega)]$ between 1.9 and 3.4 eV [compare with the real part shown in Fig. 3(a) in the same energy range]. Both previous experiments and calculations compare well with our experimental data. In Fig. 7 we show the real part of the hydrostatic component of $P_{ijkl}(\omega)$ below ~3 eV taken from Fig. 3(b) and the calculation of this function from Ref. 24. The comparison is again satisfactory. Finally, we compare in Fig. 8 previous experimental results from Ref. 23 for the real part of $[\epsilon^{\parallel}(\omega) - \epsilon^{\perp}(\omega)]/X$ when $\mathbf{X}\|[110]$, which are equivalent to $P_{44}(\omega)$ shown in Fig. 2(c).[4–6,16] There is a small difference between the $P_{44}(\omega)$ obtained when $\mathbf{X} \parallel [111]$ or $\parallel [110]$ probably due to internal stress of the samples. The experimental data of Ref. 23 for the stress-induced birefringence shown in Fig. 8 were again obtained with

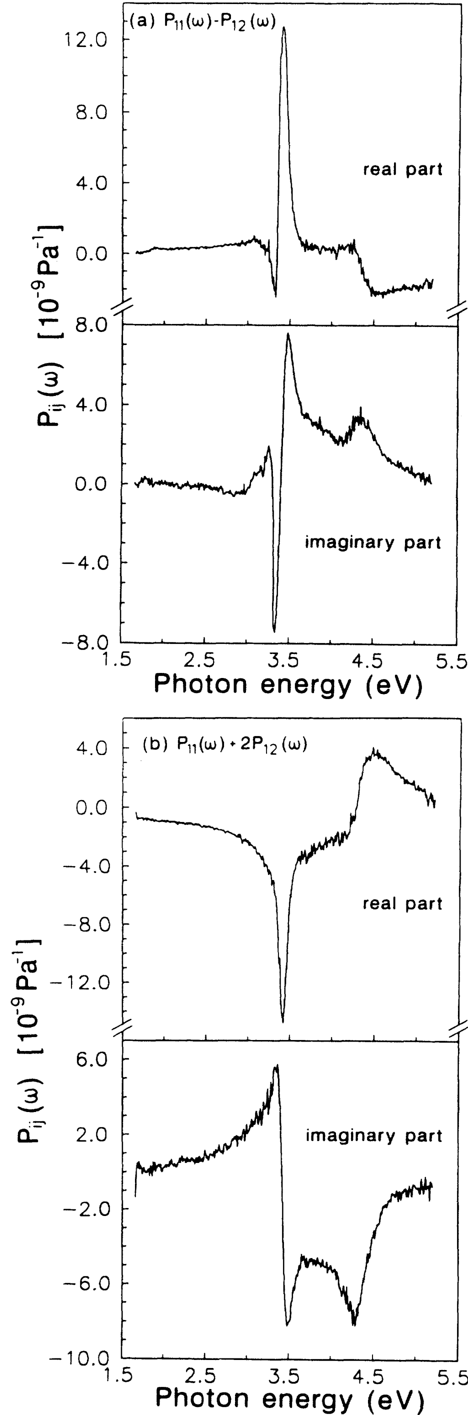

FIG. 3. (a) Γ_{12} irreducible representation of the piezo-optical tensor $P_{ijkl}(\omega)$, i.e., $[P_{11}(\omega) - P_{12}(\omega)]$ obtained from the data shown in Fig. 2. (b) Same as (a) but for the hydrostatic component $[P_{11}(\omega) + 2P_{12}(\omega)]$ (Γ_1 irreducible representation).

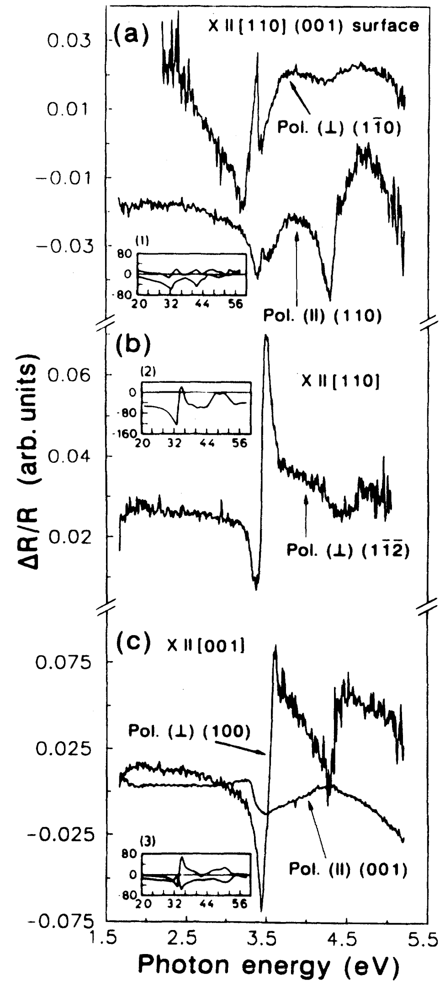

FIG. 4. Changes in the reflectivity $[\Delta R(\omega)/R(\omega)]$ calculated using the piezo-optical tensor components shown in Fig. 2. The insets are data from Ref. 16 obtained by ac-stress modulation of the reflectivity. Agreement between both sets of data is good (see the text for details).

Raman spectroscopy, in the region above 1.65 eV (where the material is opaque), and by transmission between polarizers below 1.2 eV. The comparison with previous experimental data is again satisfactory, as in Figs. 6 and 7. However, the calculations of Ref. 24 do not agree as well in this case. The $P_{44}(\omega)$ irreducible component corresponds to a strain of $\Gamma_{25'}$ symmetry which can be decomposed into an affine plus an internal deformation of the unit cell, i.e., an internal degree of freedom represented by the sublattice deformation parameter ζ.[25,26] In Fig. 3 of Ref. 24 the authors showed that the calculated $P_{44}(\omega)$ is rather sensitive to the value of ζ but were not able to obtain agreement with the experimental results for any reasonable values of that parameter. We believe that this is due to the fact that this calculation did not include exciton enhancement near the E_0' and E_1 gaps, a problem which will be discussed in the next section.

In Figs. 4–8 we showed several comparisons of the present results with previous experimental and theoret-

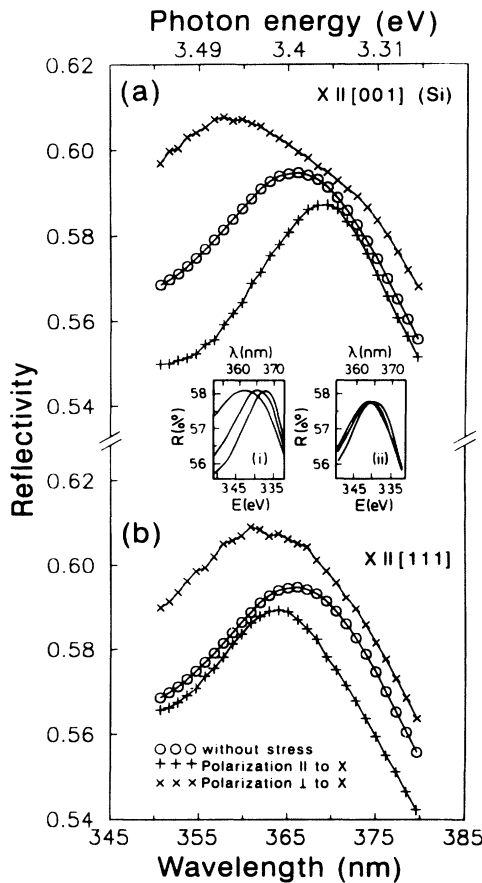

FIG. 5. (a) Absolute reflectivity for **X**=1000 MPa along [001] and polarizations $\parallel$ or $\perp$ to the stress. The parallel component is calculated from $\Delta\epsilon^{\parallel}_{\mathbf{X}\parallel[001]}(\omega) = P_{11}\cdot|\mathbf{X}|$, the perpendicular one from $\Delta\epsilon^{\perp}_{\mathbf{X}\parallel[001]}(\omega) = P_{12}\cdot|\mathbf{X}|$. The curves are slightly shifted vertically for clarity. The inset on the left shows results of polarized reflectivity from Ref. 18 for the same cases. The correspondence between the curves is obvious. (b) Same as (a) but for $\mathbf{X}\parallel[111]$; the inset on the right is the equivalent results from Ref. 18 (see Refs. 5, 6, and 18 for more details).

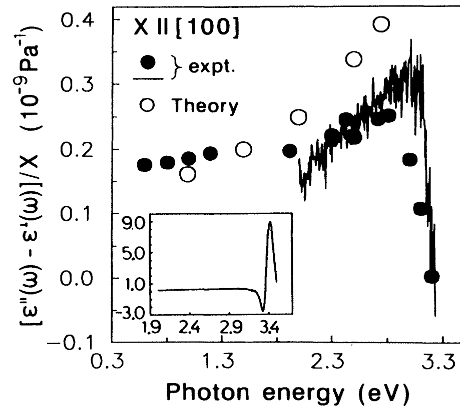

FIG. 6. Real part of $[\epsilon^{\parallel}(\omega)-\epsilon^{\perp}(\omega)]/X = [P_{11}(\omega)-P_{12}(\omega)]$ ($\mathbf{X}\parallel[100]$). The noisy line between ~1.9–3.3 eV represents our experimental data measured twice on eight different samples and averaged, thus reducing the statistical error by a factor of 4. These measurements are displayed in detail in the inset [compare with data in Fig. 3(a) for the same photon energy]. The open circles represent calculated values from Ref. 24 while the full ones are experimental data from Refs. 19–23 (see the text for details).

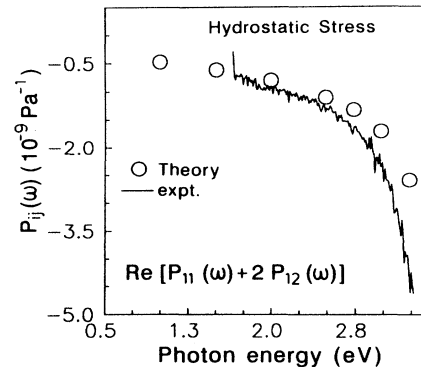

FIG. 7. Real part of the hydrostatic component extracted from Fig. 3(b) of the piezo-optic tensor. Open circles are values calculated in Ref. 24 using the so-called "scissors" operator.

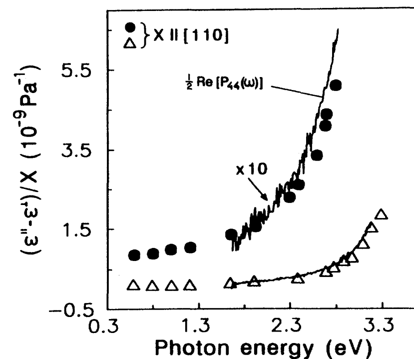

FIG. 8. Real part of $[\epsilon^{\parallel}(\omega)-\epsilon^{\perp}(\omega)]/X = -2P_{44}(\omega)$ for $\mathbf{X}\parallel[110]$. The line represents the low-energy tail of $\frac{1}{2}\mathrm{Re}[P_{44}(\omega)]$. The symbols are data from Ref. 23. The curve is shown in two different scales. Agreement with previous experimental data is good.

ical information; the agreement is satisfactory. This means that the experimental components of the tensor $P_{ijkl}(\omega)$ in Fig. 2 are able to reproduce several sets of previous results, a fact that gives additional confidence to our procedure. In the following subsection we shall concentrate on the microscopic nature of the structures between 3 and 4 eV (E_0' and E_1 gaps).

C. Structures between 3 and 4 eV

The optical structures and the effect of uniaxial stress in this photon energy region (3–4 eV) have been studied in the past, in particular by piezoreflectance techniques.[27–29] The structure exhibits fundamental differences with respect to the $(E_1 - E_1 + \Delta_1)$ gaps of Ge or GaAs (Refs. 5 and 6) which are the dominant optical structures inmediately above the lowest direct gap. According to ellipsometric data, the model pseudodielectric function of Si in this photon energy region is well represented by[30]

$$\epsilon(\omega) \sim \begin{cases} A \, \ln(\omega - E_{g_0} + i\Gamma_0)\, e^{(i\Theta_0)} & \text{for } E_0' \\ A'\,(\omega - E_{g_1} + i\Gamma_1)^{-1}\, e^{(i\Theta_1)} & \text{for } E_1, \end{cases} \tag{3}$$

where A and A' are the amplitudes (or strengths), $E_{g_{0,1}}$ the energy thresholds (or gaps), $\Gamma_{0,1}$ the broadenings, and $\Theta_{0,1}$ the phases, which take into account the excitonic character of the optical critical point.[30] The E_0' function of Eq. (3) corresponds to a two-dimensional critical point (CP) while that for E_1, a discrete Lorentzian, is sometimes called a zero-dimensional CP. As in Refs. 5 and 6, we fitted the second derivatives of $\epsilon(\omega)$ as a function of X with a model dielectric function which includes the two contributions of Eq. (3); a standard ellipsometric procedure to obtain critical-point parameters.[13,31–33] We set for the fits $\Theta_0 = \Theta_1$ (Refs. 5 and 6) and we used trial values from Refs. 32 and 33 to start the procedure. We neglect spin-orbit splitting effects, known to be small ($\leq$ 40 meV) in Si. The E_1 critical points behave under stress as shown schematically in Fig. 9.[27,28] The Λ_1 and Λ_3 bands are the orbital bands along $\{111\}$ (the four equivalent $[111], [1\bar{1}\bar{1}], [\bar{1}1\bar{1}], [\bar{1}\bar{1}1]$ directions) for the conduction and valence band, respectively.[35] For $\mathbf{X}\|[100]$ the valence bands split due to the intravalley effect of the shear strain. This, together with the hydrostatic shift (δE_H), give rise to the transitions labeled E_a and E_b in Fig. 9(a). The relative intensities shown in the figure have been calculated using a $\mathbf{k}\cdot\mathbf{p}$ scheme in Ref. 28. The eigenvalues for these two transitions as a function of the stress $X = |\mathbf{X}|$ along [100] can be shown to be[28]

$$E_a(X) = E_1(0) + \frac{D_1^1}{\sqrt{3}}\,(S_{11} + 2S_{12})\,X + \sqrt{\tfrac{2}{3}}D_3^3\,(S_{11} - S_{12})\,X \tag{4}$$

and

$$E_b(X) = E_1(0) + \frac{D_1^1}{\sqrt{3}}\,(S_{11} + 2S_{12})\,X - \sqrt{\tfrac{2}{3}}D_3^3\,(S_{11} - S_{12})\,X, \tag{5}$$

where S_{ij} are the appropriate elastic compliance constants,[34] and D_1^1, D_3^3 the hydrostatic and intraband deformation-potential constants, respectively.

For $\mathbf{X}\|[111]$ the gap along the [111] valley splits from the other three along $[1\bar{1}\bar{1}]$, $[\bar{1}1\bar{1}]$, and $[\bar{1}\bar{1}1]$, as shown schematically in Fig. 9(b). In this case there are three contributions to the gap changes depicted in Fig. 9(b) as intraband, interband, and (δE_H) (hydrostatic). The three allowed transitions are labeled as E_c, E_d, and E_e, respectively, with the following eigenvalues (with $X = |\mathbf{X}| \parallel [111]$):[28]

$$E_c(X) = E_1(0) + \frac{D_1^1}{\sqrt{3}}\,(S_{11} + 2S_{12})\,X + \frac{\sqrt{3}}{6}D_1^5 S_{44} X, \tag{6}$$

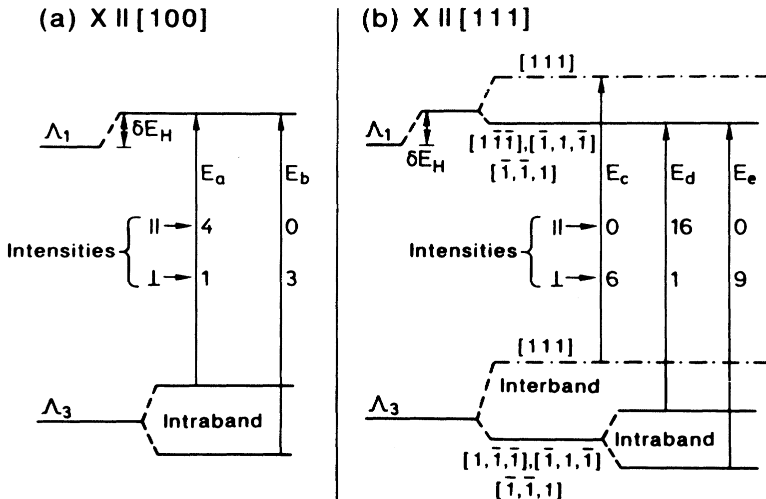

FIG. 9. Stress-induced intraband and interband splitting for different optical configurations. Λ_1 and Λ_3 are the orbital conduction and valence bands, respectively, along [111]. The intensities were calculated using $\mathbf{k}\cdot\mathbf{p}$ perturbation theory starting from the bands at Γ in Ref. 28. The eigenvalues for each case are given in the text.

$$E_d(X) = E_1(0) + \frac{D_1^1}{\sqrt{3}}(S_{11} + 2S_{12})X - \frac{D_1^5}{6\sqrt{3}}S_{44}X + \frac{\sqrt{2}}{3\sqrt{3}}D_3^5 S_{44}X, \quad (7)$$

and

$$E_e(X) = E_1(0) + \frac{D_1^1}{\sqrt{3}}(S_{11} + 2S_{12})X - \frac{D_1^5}{6\sqrt{3}}S_{44}X - \frac{\sqrt{2}}{3\sqrt{3}}D_3^5 S_{44}X, \quad (8)$$

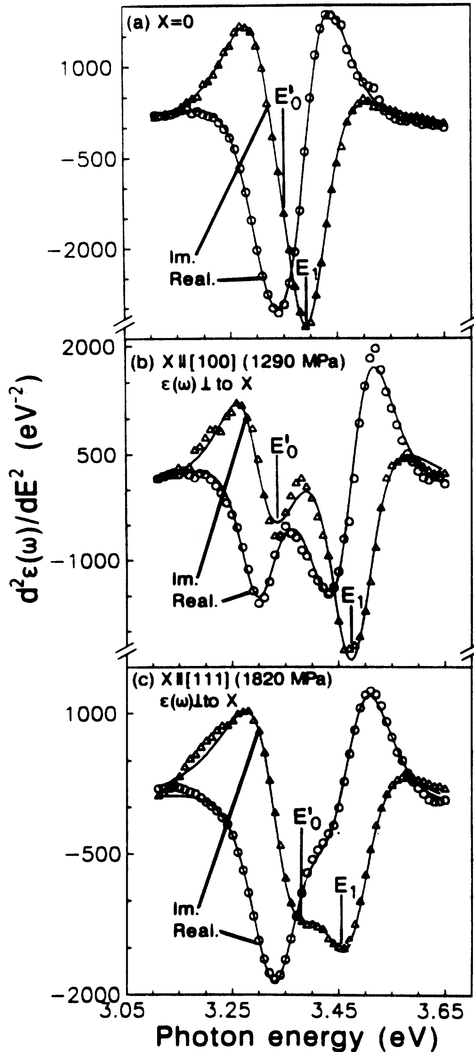

FIG. 10. Second derivatives of the pseudodielectric function $\epsilon^{\perp}(\omega)$ for (a) $\mathbf{X}$=0, (b) $\mathbf{X}\|$ [100] ($\sim$ 13 kbars), and (c) $\mathbf{X}\|$ [111] ($\sim$ 18 kbars). The symbols [real (circles) and imaginary (triangles)] were obtained by numerical differentiation of the experimental $\epsilon(\omega)$. The solid lines are best fits with a model dielectric response given by Eq. (3). In (a) both CP, E_0', and E_1 cannot be distinguished and $\mathrm{Im}\left[d^2\epsilon(\omega)/d\omega^2\right]$ reveals only one minimum. In (b) the structure is produced by the two eigenvalues E_a and E_b [Eqs. (4) and (5)] contributing to E_1 [with the relative intensities shown in Fig. 9(a)] plus E_0' which is now well discriminated. On the other hand, (c) shows the contribution of Eqs. (6)–(8) to E_1, and E_0' is less separated than in (b) [see also Figs. 11, 12(a), and 12(b)].

where the new deformation potentials, D_1^5 and D_3^5, take into account the interband and intraband contributions for a [111] stress, respectively. The relative intensities shown in Fig. 9(b) were also calculated in Ref. 28. From this energy diagram it is possible to observe that the parallel components, for both $\mathbf{X}\|$ to [111] or [100], have contributions coming from one single eigenvalue, while the perpendicular ones involve up to three different transitions (one rather weak) when stress is applied. However, the different transitions that make up E_1 in the perpendicular case cannot be resolved in our ellipsometric data. The existence of different contributions to E_1 is observed as a broadening of the peak: the samples break before the internal structure of E_1 becomes observable. For the parallel components the eigenvalues are given by E_a if $\mathbf{X}\|[100]$ or E_d if $\mathbf{X}\|[111]$, while for the perpendicular configuration the energy position of E_1 can be assumed to be a weighted average of E_a and E_b in one case ($\mathbf{X}\|[100]$), and E_c, E_d, and E_e in the other ($\mathbf{X}\|[111]$). One additional peculiarity in Si is that the energy difference between the two critical points E_0' and E_1 is small at $\mathbf{X}$=0 ($\sim$0.08 meV) while the relative strengths are $(A'/A)\sim0.2$. This causes the structure to appear as a single, somewhat asymmetric, peak.

To illustrate all these facts, we show the second derivatives of the dielectric function of the perpendicular components $\epsilon^{\perp}(\omega)$ for $\mathbf{X}$ $\|$[111] and [100], respectively, in Fig. 10. It is known[30] that for a zero- or two-dimensional critical point, the imaginary part of $d^2\epsilon(\omega)/d\omega^2$ exhibits a minimum at an energy close to that of the CP [E_g in Eq. (3)]. The minimum is not exactly at the CP energy because it depends slightly on the phase Θ. We can assert, however, that the number of minima in a given photon energy region helps in the identification of the number of critical points as well as their energies, except when the peaks are too close to be distinguished. In the latter case the peaks resemble qualitatively a single CP although the fit improves with two CP's. In Fig. 10 we

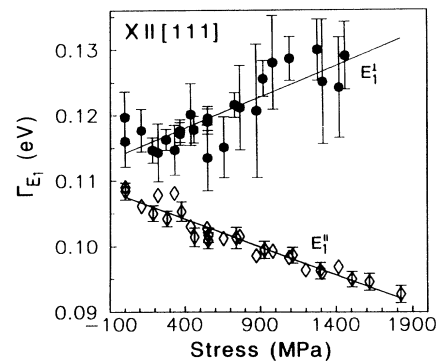

FIG. 11. Broadening of the E_1 CP for polarization $\|$ or $\perp$ to $\mathbf{X}\|[111]$. Note that for the $\|$ polarization the CP is represented by only one eigenvalue E_a and, at the same time, E_0' separates from E_1. In this case E_1 becomes a well-defined peak and the broadening diminishes. In the other case, E_1 is produced by E_c, E_d, and E_e and the peak broadens although E_0' is again being separated by means of $\mathbf{X}$ [see Figs. 12(a) and 12(b)].

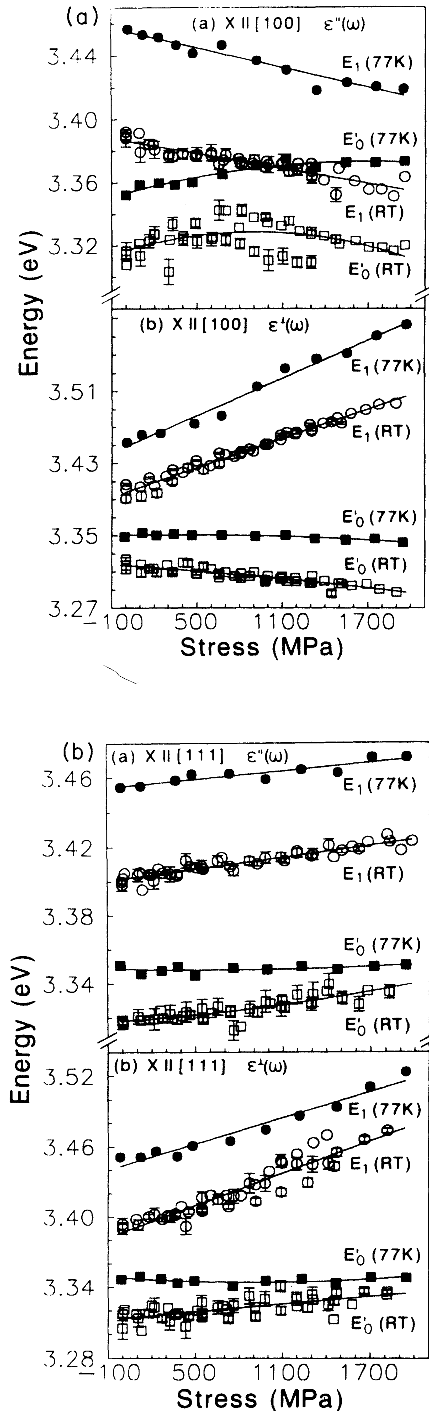

FIG. 12. (a) Critical-point energies for the E_0' and E_1 gaps of Si obtained from the fits of $\epsilon^{\parallel}(\omega)$ and $\epsilon^{\perp}(\omega)$ and $\mathbf{X}\|[100]$. The data labeled with (RT) correspond to our ellipsometric determination at room temperature. The data at 77 K were measured with wavelength-modulated reflectivity in Ref. 27. Some typical error bars are shown at some points. In the case of E_1 the lines are best linear fits for the stress dependence to obtain the deformation-potential constants (see Table I). In the case of E_0' the lines are just guides to the eye (see the text). (b) Same as (a) but for $\mathbf{X}\|[111]$.

show the experimental second derivatives of $\epsilon^{\perp}(\omega)$ for $\mathbf{X}$=0, 1290, and 1820 MPa and their best fits with the model dielectric function of Eq. (3). In Fig. 10(a), for $\mathbf{X}$=0, we observe a single minimum in $\mathrm{Im}[d^2\epsilon(\omega)/d\omega^2]$ but the fit requires both E_0' and E_1, as explained above. As the stress is increased, we can observe a clear splitting of both CP's, which is larger for $\mathbf{X}\|[100]$ than for $\mathbf{X}\|[111]$. We also show in Fig. 11 the broadenings of E_1 for both $\|$ and $\perp$ components when $\mathbf{X}\|[111]$. Note that for the parallel component, the E_1 CP is given by a single eigenvalue (7), which separates from E_0' as $\mathbf{X}$ is increased. The peak becomes well defined as a single CP and the broadening shrinks. Still, for the perpendicular component, and despite the fact that E_0' separates, E_1 has contributions from E_c, E_d, and E_e [Eqs. (6)–(8)], so that the peak broadens. That leads to the behavior shown in Fig. 11. In Figs. 12 and 13 we display the complete series of critical-point energies at room temperature obtained from the fits as a function of $\mathbf{X}$. In Fig. 12(a) we display the data for E_0' and E_1 obtained from the fits of $\epsilon^{\parallel}(\omega)$ and $\epsilon^{\perp}(\omega)$ when $\mathbf{X}\|[100]$. In Fig. 12(b) we plot the equivalent results for $\mathbf{X}\|[111]$. The data are labeled as E_0'(RT) and E_1(RT). Some typical error bars are shown; they represent only errors in the parameters of the fit. The full symbols are data at 77 K for the same gaps obtained by means of wavelength-modulated reflectivity in Ref. 27. The following distinctive features can be observed: the difference between E_0'(RT) and E_0'(77 K) at $\mathbf{X}$=0 is ~0.03 meV while that between E_1(RT) and E_1(77 K) is ~ 0.07 meV. This is in agreement with what was observed and calculated in Ref. 32. The energies E_1 are linear in the entire stress range, for all possible configurations, as expected from Eqs. (4)–(8). These curves can be used to obtain the deformation-potential constants as done in Refs. 5, 6, 27, and 36. Note that the difference between the slopes of E_1(RT) and E_1(77 K) are small in any case, leading to values of D_j^i which are similar to those reported in Ref. 27. A comparison with previous experimental values for the deformation-potential constants of the E_1 gap is given in Table I. The

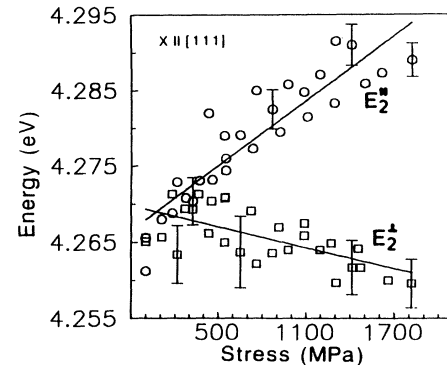

FIG. 13. E_2 energies obtained from the parallel or perpendicular component of $\epsilon(\omega)$ for $\mathbf{X}\|[111]$. From the two fitted lines and using the definition $(E_2^{\parallel} + 2E_2^{\perp}) = D_1^1(E_2)/\sqrt{3}(S_{11} + 2S_{12})X$, the hydrostatic deformation-potential constant $D_1^1(E_2)$ of Table I was obtained.

TABLE I. Deformation-potential constants for the E_1 and E_2 gaps of Si, compared with those obtained in other measurements and theoretical estimates.

D_1^1	D_1^5	D_3^3 (eV)	D_3^5 (eV)	$D_1^1(E_2)$	Exp. conditions	Reference
-9.8 ± 1.3	6.5 ± 1.4	4.7 ± 0.5	3.0 ± 1.7		(77 K) Electroreflectance	29
-8 ± 1	10 ± 2	5 ± 1	4 ± 1		(77 K) Wavelength-mod. reflectivity	27
-8.7 ± 1.3	11 ± 3	4.2 ± 0.3	5.3 ± 1.9		(RT) Ellipsometry	45
-9.72 ± 0.56	7.83 ± 0.55	4.36 ± 0.62	5.04 ± 0.87	2.6 ± 1.1	(RT) Ellipsometry	present work
-9.31	7.05	4.3	6.28		Pseudopotential method	present work

features displayed by E_0' are more involved, in particular for the stress dependence of E_0' obtained from $\epsilon^{\|}(\omega)$ when $\mathbf{X}\|[100]$ [Fig. 12(a)]. There is a clear nonlinearity in the energy dependence which was also observed at 77 K in Ref. 27 [see E_0'(77 K) in Fig. 12(a)]. Since the slopes of E_1 and E_0' are of opposite signs and the gaps tend to join, one might conjecture that this curvature arises from a repulsive interaction with E_1. But, since E_1 shows no upwards curvature, interaction with possible forbidden exciton components of E_0' (split by exchange interaction) can also be conjectured. Microscopic calculations of the excitonic excitation spectrum,[41,42] including dipole-forbidden components, are not available but would be desirable to clarify this point. A good starting point to clarify this feature is to note that when using the excitonic basis of wave functions to represent the optical transitions at $\mathbf{k} = 0$, the splitting between the optically active Γ_{15} modes and the coupling to the exchange split inactive ones depends essentially on the difference between the corresponding deformation potentials (which are different depending on whether $\mathbf{X}$ is parallel to [100] or [111]). Calculation of this deformation potential at $\mathbf{k} = 0$ have been performed by the pseudopotential method in Ref. 44. The trend obtained from the calculated values is in agreement with this picture. One finds for $\mathbf{X}\|[100]$ (using the notation of Ref. 44 for the deformation potentials that was introduced by Pikus[1]) $b_c - b_v$=3.5 eV and for $\mathbf{X}\|[111]$ $d_c - d_v \sim 0$. This implies that for a [111] stress the E_0' exciton should not split nor couple to the dipole-forbidden components. However, for a [100] stress $b_c - b_v \neq 0$ and splitting and coupling should result. This agrees with the results of Fig. 12. Finally, for the sake of completeness, we show in Fig. 13 the analysis of the E_2 for the case of $\mathbf{X}\|[111]$. E_2 is expected to behave hydrostatically since its origin lies in a broad region of the first Brillouin zone. The origin of this critical point has been assigned to large regions near $\mathbf{k} = (0.50, 0.25, 0.25) \times 2\pi/a$ and an analysis of the shear contributions to this peak may require more extensive calculations than the ones we are going to present in the following section. However, a hydrostatic deformation-potential constant from the data of Fig. 13 can always be obtained regardless of whether shear contributions are present or not. The value so obtained is displayed in Table I.

III. THEORY

We have calculated using the empirical pseudopotential method[37–40] the three independent components of the piezo-optical tensor $P_{ijkl}(\omega)$ in the same photon energy region as the experiment. The same procedure was followed for Ge and GaAs in Refs. 5 and 6. A few details of the calculation are given in this section.

The method used to interpolate the Fourier components of the pseudopotential[37,38] was given in Refs. 5 and 6. The Fourier coefficients for the unstressed lattice were obtained from Ref. 39. The lattice parameters and elastic compliance constants at RT were taken from Ref. 34. We used 2361 points within the full first Brillouin zone (BZ) as in Refs. 5 and 6. The calculation has been performed without spin-orbit coupling, which should be much better justified for Si than in Refs. 5 and 6 for Ge and GaAs. The external stress had to be taken as high as 4 GPa, to avoid numerical problems with small differences. The imaginary part of $\epsilon(\omega)$ was computed with Eq. (24) of Ref. 5 (see also Ref. 37). In Fig. 14 we compare the calculated imaginary part of $\epsilon(\omega)$ for $\mathbf{X}$=0 with the experimental one extracted from Fig. 1. As is expected,[5,6,37–39,41,42] the calculated imaginary part of $\epsilon(\omega)$ in the region around $\sim$ 3.5 eV (E_0' and E_1 gaps) is too small when compared with the experiment, as a result of not having included excitonic interaction.[41,42] This is illustrated in the inset of Fig. 14, where three different imaginary parts, calculated with different approaches, are shown.[41,42] The curve labeled $\bar{\epsilon}(\omega)$ was calculated in the one-electron approximation without local field cor-

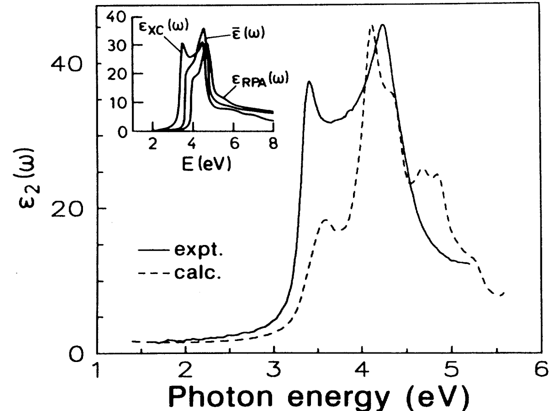

FIG. 14. Experimental (RAE) and calculated (EPM) imaginary parts of $\epsilon(\omega)$ for $\mathbf{X}$=0. Note the difference between the measured and the calculated values around $\sim$ 3.5 eV. The inset displays three different calculations of $\epsilon_2(\omega)$ (Hartree approximation [$\bar{\epsilon}(\omega)$], RPA [$\epsilon_{RPA}(\omega)$], and RPA plus screened exchange interaction $\epsilon_{XC}(\omega)$). The exciton enhancement is clearly seen in the latter.

rections and corresponds, essentially, to our result. The two other results are $\epsilon_{\rm RPA}(\omega)$, calculated within the RPA with local field corrections, and $\epsilon_{\rm XC}(\omega)$, calculated with local field plus screened exchange correction (corresponding to excitonic interaction).[42] Note the "excitonic" enhancement in the region ~ 3.5 eV in the latter. Instead of adding new parameters to our calculation of $P_{ijkl}(\omega)$, we performed it without excitonic enhancement and multiplied the final result by $\epsilon_{\rm expt}(\omega)/\epsilon_{\rm calc}(\omega)$ so that the exciton contribution is taken into account "by hand." For stress along [111] we used an internal strain parameter $\zeta = 0.564$ (see Ref. 24). The calculated curves (imaginary parts) are compared with the experiment in Fig. 15. The agreement is remarkably good, especially considering the crude approximations involved. Similar results were presented in Refs. 5 and 6 for Ge and GaAs. If the values of Ref. 24 were corrected for exciton enhancement (roughly a factor of ~ 2 for the 3.5-eV contribution), the disagreements with the experimental results would have virtually disappeared. Without going into details, we only mention in this respect that exciton enhancement affects $P_{44}(\omega)$ in this case more than the other components: hence the discrepancy pointed out by the authors of Ref. 24. Also the "scissors-operator" approach assumes a rigid shift of the conduction band to fit the experimentally observed gap, formally achieved by adding to the local-density-approximation Hamiltonian $\hat{\mathbf{H}}_{\mathbf{k}}^{\rm LDA}$ a term representing the shift, i.e.,[24]

$$\hat{\mathbf{H}} \rightarrow \hat{\mathbf{H}}_{\mathbf{k}}^{\rm LDA} + \Delta_{\mathbf{k}} P_{c,\mathbf{k}}, \tag{9}$$

where $\Delta_{\mathbf{k}}$ represents the energy shift of the conduction bands and $P_{c,\mathbf{k}}$ projects the wave functions onto the conduction band at $\mathbf{k}$.[24] This approach is open to criticism and seems to fail in representing the modulated response above 3 eV where the contribution of the higher conduction bands cannot be neglected. The EPM method, although empirical, seems to be successful in predicting effects of different perturbations including effects of the electron-phonon interaction over a broad range of energies.[43] It has been proved to be quite reliable also in the calculation of deformation potentials.[44] We performed the calculation of the deformation-potential constants of E_1 for stress $\|[100]$ [Eqs. (4) and (5)] and for $\mathbf{X}\|[111]$ [Eqs. (6)–(8)] and their $\mathbf{k}$ dependence along Λ is shown in Fig. 16. The calculation for $\mathbf{X}\|[100]$ allows us to obtain D_1^1 from the shift of the conduction band Λ_1 and D_3^3 from the splitting of the Λ_3. In the other case, $\mathbf{X}\|[111]$ [using the same ζ employed in the calculation $P_{ijkl}(\omega)$ in Fig. 15], the D_3^5 and D_1^5 deformation potentials can be obtained.[2] The interband deformation potential D_1^5 has been separated into the two contributions of the valence and the conduction bands. All the values displayed in Table I are averages from $\mathbf{k} = 0$ to the zone boundary along $\Lambda = \langle 111 \rangle$. The agreement with the experiment is excellent.

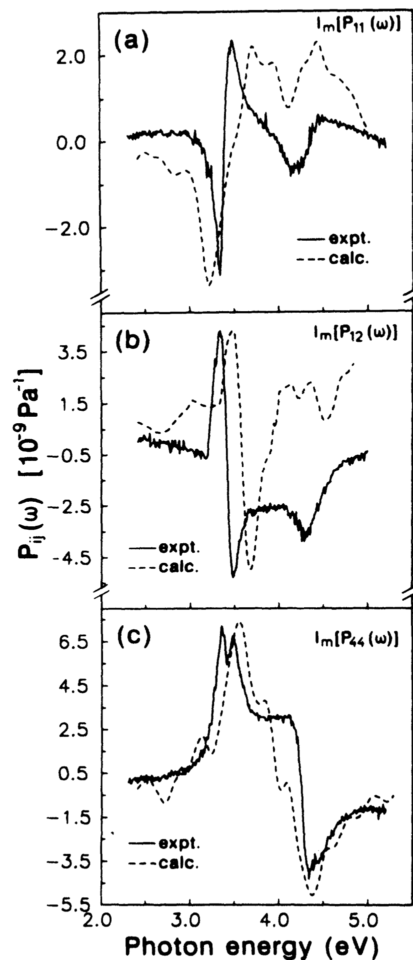

FIG. 15. Comparison between theory (EPM, dashed lines) and experiment (solid lines) for the imaginary parts of the three independent components of $P_{ijkl}(\omega)$. The calculation has been performed as explained in the text (see also Refs. 5, 6, and 24 for similar results).

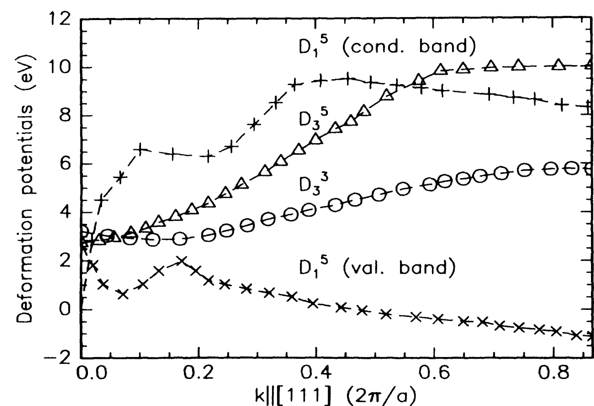

FIG. 16. Deformation-potential constants for transitions along Λ. For $\mathbf{X}\|[100]$ the analysis of the valence-band splitting leads to the D_3^3 plot in the figure. The case of $\mathbf{X}\|[111]$ is represented by the deformation potentials D_3^5 and D_1^5. D_3^5 (intraband term if Fig. 9) comes from Λ_3 alone, but D_1^5 has been separated into the interband contribution for Λ_1 (conduction band) and Λ_3 (valence band). The values displayed in Table I are averages from $\mathbf{k} = 0$ to the zone boundary along Λ.

IV. CONCLUSIONS

We have determined the piezo-optical tensor of Si using rotating-analyzer ellipsometry following our previous works on Ge and GaAs.[5,6] The results of this paper are able to reproduce previous experimental results and also compare well with calculations. From the experimental point of view, the previous experimental works on the piezo-optical response of Si in the visible are almost restricted to Refs. 16 and 18. In the case of recent *ab initio* calculations[24] the reason for the lack of agreement with experiments has been clarified. In addition, our results solve some contradictions and errors in the existing literature concerning the analysis of piezoreflectance data. The agreement in the low-energy tail of $P_{ijkl}(\omega)$ with previous experimental work is excellent. To our knowledge, these are the first reliable data of $P_{ijkl}(\omega)$ in the visible and near-uv region obtained without artificial manipulation of raw data. In that sense, ellipsometry provides a powerful tool for the determination of the piezo-optical response of semiconductors as we also have already shown in Refs. 5 and 6. Open questions are the stress dependence of E_0' and the calculation of $P_{ijkl}(\omega)$ within the framework of a first-principles method including excitonic contributions. A similar work on GaP and InP is in progress and will be published elsewhere.[46]

Note added in proof. The hydrostatic component $P_{11}(\omega) + 2P_{12}(\omega)$ shown in Fig. 3(b) was obtained from measurements under [111] stress. Nearly identical (within the experimental error) results were obtained from the data for [100] stress thus providing an additional proof of self-consistency of the data. The same applies to the Ge results of Ref. 5. In the case of GaAs the $P_{11}(\omega) + 2P_{12}(\omega)$ data of Ref. 6, obtained for [111] stress, are believed to be correct. However, they disagree somewhat with those obtained from [100] stress. This topic is currently being investigated.

ACKNOWLEDGMENTS

Thanks are due to H. Hirt, M. Siemers, and P. Wurster for expert technical help during the experiments. The original codes to analyze the ellipsometric data were written by M. Garriga (Ref. 11) with whom we had enlightening discussions throughout the experiments. The EPM code is based on an original program written by C. Grein (Refs. 5 and 6). It is a pleasure to thank Paulo Santos for a critical reading of the manuscript.

*Present address: Department of Physics, University of California, Berkeley, CA 74720.

[1] G. L. Bir and G. E. Pikus, in *Symmetry and Strain-Induced Effects in Semiconductors*, edited by D. Louvish (Wiley, New York, 1974).

[2] E. O. Kane, Phys. Rev. **178**, 1368 (1969), and references therein.

[3] F. Pollak, Surf. Sci. **37**, 863 (1973).

[4] I. Balslev, in *Semiconductors and Semimetals*, edited by R. K. Willardson and A. C. Beer (Academic, New York, 1972), Vol. 9.

[5] P. Etchegoin, J. Kircher, M. Cardona, and C. Grein, Phys. Rev. B **45**, 11 721 (1992).

[6] P. Etchegoin, J. Kircher, M. Cardona, C. Grein, and E. Bustarret, Phys. Rev. B **46**, 15 139 (1992).

[7] D. E. Aspnes and A. A. Studna, Rev. Sci. Instrum. **49**, 292 (1978).

[8] R. M. Azzam and N. M. Bashara, *Ellipsometry and Polarized Light* (North-Holland, Amsterdam, 1977).

[9] D. S. Kliger, J. W. Lewis, and C. E. Randall, *Polarized Light in Optics and Spectroscopy* (Academic, Boston, 1990).

[10] D. E. Aspnes, J. Opt. Soc. Am. **70**, 1275 (1980).

[11] M. Garriga, Ph.D. thesis, University of Stuttgart, 1990.

[12] J. Kircher, W. Böhringer, W. Dietrich, H. Hirt, P. Etchegoin, and M. Cardona, Rev. Sci. Instrum. **63**, 3733 (1992).

[13] D. E. Aspnes and A. A. Studna, Phys. Rev. B **27**, 985 (1983).

[14] D. E. Aspnes and A. A. Studna, Appl. Phys. Lett. **39**, 316 (1981).

[15] V. Nayar, W. Y. Leong, C. Pickering, A. J. Pidduck, R. T. Carline, and D. J. Robbins, Appl. Phys. Lett. **61**, 1304 (1992).

[16] G. W. Gobeli and E. O. Kane, Phys. Rev. Lett. **15**, 142 (1965).

[17] M. Cardona, in *Modulation Spectroscopy of Solids*, edited by H. Ehrenreich, F. Seitz, and D. Turnbull (Academic, New York, 1969).

[18] U. Gerhardt, Phys. Rev. Lett. **15**, 401 (1965).

[19] D. K. Biegelsen, Phys. Rev. Lett. **32**, 1196 (1974).

[20] C. W. Higginbotham, M. Cardona, and F. H. Pollak, Phys. Rev. B **18**, 4301 (1978).

[21] M. H. Grimsditch, E. Kisela, and M. Cardona, Phys. Status Solidi A **60**, 135 (1980).

[22] D. K. Biegelsen, Phys. Rev. B **12**, 2427 (1975).

[23] M. Chandrasekhar, M. H. Grimsditch, and M. Cardona, Phys. Rev. B **18**, 4301 (1978).

[24] Z. H. Levine, H. Zhong, S. Wei, D. C. Allan, and J. W. Wilkins, Phys. Rev. B **45**, 4131 (1992). In this reference a different definition of the piezooptical tensor is used but can be converted to our's knowing the elastic compliance constants and the frequency-dependent index of refraction $n(\omega)$.

[25] L. Kleinman, Phys. Rev. **128**, 2614 (1962).

[26] C. S. G. Cousins, J. Phys. C **15**, 1857 (1982).

[27] F. H. Pollak and G. W. Rubloff, Phys. Rev. Lett. **29**, 789 (1972).

[28] F. H. Pollak and M. Cardona, Phys. Rev. **172**, 816 (1968).

[29] K. Kondo and A. Moritani, Phys. Rev. B **14**, 1577 (1976).

[30] D. E. Aspnes, in *Handbook on Semiconductors*, edited by T. S. Moss and M. Balkanski (North-Holland, Amsterdam, 1980), p. 110.

[31] C. C. Kim, J. W. Garland, H. Abad, and P. M. Raccah, Phys. Rev. B **45**, 11 749 (1992).

[32] P. Lautenschager, P. B. Allen, and M. Cardona, Phys. Rev. B **31**, 2163 (1985).

[33] P Lautenschager, M. Garriga, L. Viña, and M. Cardona, Phys. Rev. B **36**, 4821 (1987).

[34] R. F. S. Hearmon, in *Elastic, Piezoelectric and Related Constants of Crystals*, edited by K. H. Hellwege and A. M. Hellwege, Landolt-Börnstein, New Series, Group III, Vol. 11 (Springer-Verlag, Berlin, 1969), p. 11.

[35] M. Cardona, in *Atomic Structure and Properties of Solids*, edited by E. Burstein (Academic, New York, 1972),

p. 513.
[36]M. Chandrasekhar and F. Pollak, Phys. Rev. B **15**, 2127 (1977).
[37]M. L. Cohen and J. R. Chelikosky, in *Electronic Structure and Optical Properties of Semiconductors*, edited by M. Cardona, Springer Series in Solid-State Science Vol. 75 (Springer-Verlag, Berlin, 1988).
[38]M. L. Cohen and V. Heine, in *Solid State Physics*, edited by H. Ehrenreich, F. Seitz, and D. Turnbull (Academic, New York, 1970), Vol. 24.
[39]M. L. Cohen and T. Bergstresser, Phys. Rev. **141**, 789 (1966).
[40]L. Saravia and D. Brust, Phys. Rev. **171**, 916 (1968).
[41]W. Hanke and L. J. Sham, Phys. Rev. Lett. **33**, 582 (1974).
[42]W. Hanke and L. J. Sham, in *Physics of Semiconductors 1978*, edited by B. L. H. Wilson (The Institute of Physics, London, 1979), p. 1367.
[43]S. Zollner, M. Cardona, and S. Gopalan, Phys. Rev. B **45**, 3376 (1992).
[44]A. Blacha, H. Presting, and M. Cardona, Phys. Status Solidi B **126**, 11 (1984).
[45]M. Garriga (private communication).
[46]P. Etchegoin, J. Kircher, and M. Cardona (unpublished).